Magnetic Vortex Dynamics Induced by an Electrical Current

YURI GAIDIDEI,[1] VOLODYMYR P. KRAVCHUK,[1] DENIS D. SHEKA[2]

[1]*Institute for Theoretical Physics, 03680 Kiev, Ukraine*
[2]*National Taras Shevchenko University of Kiev, 03127 Kiev, Ukraine*

Received 13 January 2009; accepted 10 March 2009
Published online 3 June 2009 in Wiley InterScience (www.interscience.wiley.com).
DOI 10.1002/qua.22253

ABSTRACT: A magnetic nanoparticle in a vortex state is a promising candidate for the information storage. One bit of information corresponds to the upward or downward magnetization of the vortex core (vortex polarity). The dynamics of the magnetic vortex driven by a spin current is studied theoretically. Using a simple analytical model and numerical simulations, we show that a nondecaying vortex motion can be excited by a dc spin–polarized current, whose intensity exceeds a first threshold value as a result of the balance between a spin-torque pumping and damping forces. The irreversible switching of the vortex polarity takes place for a current above a second threshold. The mechanism of the switching, which involves the process of creation and annihilation of a vortex–antivortex pair is described analytically, using a rigid model, and confirmed by detailed spin–lattice simulations. © 2009 Wiley Periodicals, Inc. Int J Quantum Chem 110: 83–97, 2010

Key words: magnetic vortex; vortex polarity; micromagnetism; spin-polarized current

1. Introduction

A strikingly rapid development of the elementary base of systems of information storage and processing causes the change over to magnetic particles and their structures with typical scales less than a micron. It is important to manipulate very fast by magnetic properties of such systems. Investigations of magnetic nanostructures include studies of magnetic nanodots, that is, submicron disk-shaped particles, which have a single vortex in the ground state due to the competition between exchange and magnetic dipole–dipole interaction. A vortex state is obtained in nanodots that are larger than a single domain whose size is a few nanometers: for example, for the Permalloy ($Ni_{80}Fe_{20}$) nanodot, the exchange length l_{ex} ~6 nm. Magnetic nanodots with their vortex ground state show a considerable promise as candidates for high density magnetic storage and high

Correspondence to: V. P. Kravchuk; e-mail: vkravchuk@bitp.kiev.ua

Contract grant sponsor: Deutsches Zentrum für Luft- und Raumfart e.V., Internationales Büro des Bundesministeriums für Forschung und Technologie, Bonn, in the frame of a bilateral scientific cooperation between Ukraine and Germany.

Contract grant number: UKR 05/055.

Contract grant sponsor: Fundamental Researches State Fund of Ukraine.

Contract grant number: F25.2/081.

© 2009 Wiley Periodicals, Inc.

speed nonvolatile magnetic random access memory (MRAM) and spin-torque random access memory (STRAM). The vortex state disks are characterized by the following conserved quantities, which can be associated with a bit of information: the polarity, the sense of the vortex core magnetization direction (up or down), and the chirality or handedness, the sense of the in–plane curling direction of the magnetization (clockwise or counterclockwise). That is why one needs to control magnetization reversal, a process in which vortices play a big role [1]. Great progress has been made recently with the possibility to observe high frequency dynamical properties of the vortex state in magnetic dots by Brillouin light scattering of spin waves [2, 3], time-resolved Kerr microscopy [4], phase sensitive Fourier transformation technique [5], X-ray imaging technique [6], and micro-SQUID technique [7].

The control of magnetic nonlinear structures using an electrical current is of special interest for applications in spintronics [8–11]. The spin–torque effect, which is the change of magnetization due to the interaction with an electrical current, was predicted by Slonczewski [12] and Berger [13] in 1996. During the last decade, this effect was tested in different magnetic systems [14–33]. Nowadays, the spin–torque effect plays an important role in spintronics [9, 10]. Recently, the spin torque effect was observed in vortex state nanoparticles. In particular, circular vortex motion can be excited by an AC [34] or a DC [31, 35, 36] spin-polarized current. Very recently it was predicted theoretically [37, 38] and observed experimentally [32] that the vortex polarity can be controlled using a spin-polarized current. This opens up the possibility of realizing electrically controlled magnetic devices, changing the direction of modern spintronics [39].

We show that the spin current causes a nontrivial vortex dynamics. When the current strength exceeds some threshold value $j_{\rm cr}$, the vortex starts to move along a spiral trajectory, which converges to a circular limit cycle. When the current strength exceeds the second threshold value $j_{\rm sw}$, the vortex switches its polarity during its spiral motion. After that it rapidly goes back to the dot center. We present a simple picture of this switching process and confirm our results by spin-lattice simulations.

2. Model and Continuum Description

We start from the model of the classical ferromagnetic system with a Hamiltonian $\mathcal{H}$, described by the isotropic Heisenberg exchange interaction $\mathcal{H}^{\rm ex}$, on–site anisotropy $\mathcal{H}^{\rm an}$, and the dipolar interaction $\mathcal{H}^{\rm dip}$:

$$\mathcal{H} = -\frac{J}{2}\sum_{(n,\delta)} \boldsymbol{S}_n \cdot \boldsymbol{S}_{n+\delta} + \mathcal{K}\sum_n \left(S_n^z\right)^2 + \frac{D}{2}\sum_{\substack{n,n'\\ n\neq n'}} \frac{\boldsymbol{S}_n\cdot\boldsymbol{S}_{n'} - 3(\boldsymbol{S}_n\cdot\boldsymbol{e}_{nn'})(\boldsymbol{S}_{n'}\cdot\boldsymbol{e}_{nn'})}{|\boldsymbol{n}-\boldsymbol{n}'|^3}. \quad (1)$$

Here $\boldsymbol{S}_n \equiv (S_n^x, S_n^y, S_n^z)$ is a classical spin vector with fixed length S in units of action on the site $\boldsymbol{n} = (n_x, n_y, n_z)$ of a three–dimensional cubic lattice with integers n_x, n_y, n_z, J is the exchange integral, $\mathcal{K}$ is the on–site anisotropy constant, the parameter $D = \gamma^2/a^3$ is the strength of the long–range dipolar interaction, $\gamma = g|e|/(2mc)$ is a gyromagnetic ratio, g is the Landé–factor, a is the lattice constant; the vector $\boldsymbol{\delta}$ connects nearest neighbors, and $\boldsymbol{e}_{nn'} \equiv (\boldsymbol{n}-\boldsymbol{n}')/|\boldsymbol{n}-\boldsymbol{n}'|$ is a unit vector. The spin dynamics of the system is described by the discrete version of the Landau—Lifshitz—Gilbert (LLG) equation

$$\frac{d\boldsymbol{S}_n}{dt} = -\left[\boldsymbol{S}_n \times \frac{\partial\mathcal{H}}{\partial\boldsymbol{S}_n}\right] - \frac{\alpha}{S}\left[\boldsymbol{S}_n \times \frac{d\boldsymbol{S}_n}{dt}\right]. \quad (2)$$

The continuum dynamics of the the spin system can be describes in terms of magnetization vector $\boldsymbol{M}$. The energy functional

$$E = \int d\boldsymbol{r}\left[\frac{A}{2M_S^2}(\nabla\boldsymbol{M})^2 + KM_z^2 - \frac{1}{2}(\boldsymbol{M}\cdot\boldsymbol{H}^{\rm ms})\right], \quad (3)$$

where $A = 2JS^2/a$ is the exchange constant, $M_{\rm S} = \gamma S/a^3$ is the saturation magnetization, $K = \mathcal{K}/(a^3\gamma^2)$, and $\boldsymbol{H}^{\rm ms}$ is a magnetostatic field, which comes from the dipolar interaction. Magnetostatic field $\boldsymbol{H}^{\rm ms}$ satisfies the Maxwell magnetostatic equations [40, 41]

$$\begin{cases} \nabla\times\boldsymbol{H}^{\rm ms} = 0, \\ \nabla\cdot\boldsymbol{H}^{\rm ms} = -4\pi\nabla\cdot\boldsymbol{M}, \end{cases} \quad (4)$$

which can be solved using magnetostatic potential, $\boldsymbol{H}^{\rm ms} = -\nabla\Phi^{\rm ms}$. The source of the field $\boldsymbol{H}^{\rm ms}$ are magnetostatic charges: volume charges $\lambda^{\rm ms} \equiv -\nabla\cdot\boldsymbol{m}$ and surface ones $\sigma^{\rm ms} \equiv \boldsymbol{m}\cdot\boldsymbol{n}$ with $\boldsymbol{m} = \boldsymbol{M}/M_{\rm S}$ and $\boldsymbol{n}$ being the external normal. The magnetostatic

potential inside the sample and energy read:

$$\Phi^{\rm ms}(\boldsymbol{r}) = M_S\left(\int_V d\boldsymbol{r}'\frac{\lambda^{\rm ms}(\boldsymbol{r}')}{|\boldsymbol{r}-\boldsymbol{r}'|}+\int_S dS'\frac{\sigma^{\rm ms}(\boldsymbol{r}')}{|\boldsymbol{r}-\boldsymbol{r}'|}\right), \quad (5a)$$

$$E^{\rm ms} = \frac{M_{\rm S}}{2}\left(\int_V d\boldsymbol{r}\lambda^{\rm ms}(\boldsymbol{r})\Phi^{\rm ms}(\boldsymbol{r})+\int_S dS\sigma^{\rm ms}(\boldsymbol{r})\Phi^{\rm ms}(\boldsymbol{r})\right). \quad (5b)$$

The evolution of magnetization can be described by the continuum version of Eq. (2). In terms of the angular variables $\boldsymbol{m} = (\sin\theta\cos\phi, \sin\theta\sin\phi, \cos\theta)$ these LLG equations read:

$$\sin\theta\,\partial_\tau\phi = -\frac{\delta\mathscr{E}}{\delta\theta} - \alpha\,\partial_\tau\theta, \quad (6a)$$

$$-\sin\theta\,\partial_\tau\theta = -\frac{\delta\mathscr{E}}{\delta\phi} - \alpha\sin^2\theta\,\partial_\tau\phi. \quad (6b)$$

Here and below

$$\tau = \omega_0 t, \quad \mathscr{E} = \frac{E}{4\pi M_{\rm S}^2}, \quad \omega_0 = 4\pi\gamma M_{\rm S}. \quad (7)$$

3. Magnetic Vortex in the Nanodisk

Magnetic properties of small particles can be described by the macrospin approximation [42] only when the typical particle size does not exceed the exchange length

$$\ell = \sqrt{\frac{A}{4\pi M_{\rm S}^2}}, \quad (8)$$

which is about $5\div10$ nm for typical magnetically soft materials [40]. When the particle increases, the magnetization curling becomes energetically preferable due to the competition between the exchange and dipolar interaction. There appears a domain structure with a typical size defined by the magnetic length $l_0 = \sqrt{A/|K|}$. Another type of the nonuniform magnetization structure appears in magnetic particles of soft magnets with $|K|/M_{\rm S}^2 \ll 1$, namely nonuniform structures with closed magnetic flux due to the dipolar interaction [40, 41].

We consider the disk–shape particle of the radius L and the thickness h. The ground state of the small size nanodisk is quasi–uniform; it depends on the particle aspect ratio $\varepsilon = h/2L$: thin nanodisks are magnetized in the plane (when $\varepsilon < \varepsilon_{\rm c} \approx 0.906$) [43] and thick ones along the axis (when $\varepsilon > \varepsilon_{\rm c}$). When the particle size exceed some critical value, which depends on the thickness, the magnetization curlingbecomes energetically preferable due to the competition between the exchange and dipolar interaction. For the disk shape particle, there appears the vortex state. The static vortex state provides the absence of volume and edge surface magnetostatic charges. The only small stray field comes from face surface charges, which are localized inside the core. For thin disks, the magnetization distribution does not depend on the thickness coordinate z. The static vortex configuration has the following form

$$\cos\theta = pm_z(r), \qquad \phi = q\chi + \mathfrak{C}\pi/2. \quad (9)$$

Here $q = 1$ is the π^1 topological charge (vorticity), $p = \pm1$ describes the vortex core magnetization, that is, the vortex polarity (up or down), $\mathfrak{C} = \pm1$ describes the in–plane curling direction of the magnetization, that is, its chirality (clockwise or counterclockwise). The vortex polarity is connected to the π_2 topological properties of the system, the Pontryagin index,

$$Q = \frac{\epsilon_{ij}}{8\pi}\int d^2x\boldsymbol{m}\cdot[\partial_i\boldsymbol{m}\times\partial_j\boldsymbol{m}] = \frac{qp}{2}. \quad (10)$$

The exchange energy of the vortex takes a form

$$W^{\rm ex} \equiv \frac{E^{\rm ex}}{VM_{\rm S}^2} = \frac{4\pi\ell^2}{L^2}\int_0^1\rho d\rho\left[\theta'(\rho)^2+\frac{\sin^2\theta(\rho)}{\rho^2}\right], \quad \rho\equiv\frac{r}{L}. \quad (11)$$

The magnetostatic energy of the vortex is caused by the magnetostatic charges; for the static vortex configuration (9) both volume and edge surface charges are absent [40]. The magnetostatic energy of the vortex is only due to the face surface charges $\sigma_{\rm face}^{\rm ms} = m_z(\rho)$, and the magnetostatic energy takes a form [44]

$$W^{\rm ms} \equiv \frac{E^{\rm ms}}{VM_{\rm S}^2} = \int_0^1\rho d\rho\int_0^1\rho' d\rho' m_z(\rho)m_z(\rho')\mathscr{K}(\rho,\rho'), \quad (12a)$$

$$\mathscr{K}(\rho,\rho') = 4\pi\int_0^\infty g(2\varepsilon x)J_0(\rho x)J_0(\rho' x)xdx, \qquad g(t)\equiv\frac{1-\exp(-t)}{t}. \quad (12b)$$

By minimizing the total energy $W^{\rm ex}+W^{\rm ms}$, one can obtain the out–of–plane vortex structure as a solution of the integro–differential equation [45]:

$$\frac{d^2\theta}{d\rho^2}+\frac{1}{\rho}\frac{d\theta}{d\rho}-\frac{\sin\theta\cos\theta}{\rho^2}+\frac{L^2}{4\pi\ell^2}\sin\theta\int_0^1\rho' d\rho'\cos\theta(\rho')\mathscr{K}(\rho,\rho')=0, \quad (13)$$

which can be solved numerically only. In the limit of infinitesimally thin disk ($\varepsilon \ll 1$), the kernel takes a local form, $\mathscr{K}(\rho,\rho')=4\pi\delta(\rho-\rho')/\rho$ [45], hence

$$W^{\mathrm{ms}}=4\pi\int_0^1\rho d\rho\cos^2\theta(\rho), \quad (14)$$

which coincides with energy of the easy–plane anisotropy. Therefore, the vortex structure can be approximately described by the ODE [44]

$$\frac{d^2\theta}{d\rho^2}+\frac{1}{\rho}\frac{d\theta}{d\rho}+\sin\theta\cos\theta\left[\left(\frac{L}{\ell}\right)^2-\frac{1}{\rho^2}\right]=0. \quad (15)$$

Let us discuss the behavior of $\theta(\rho)$. The standard way to analyze the vortex structure is to use some ansatz instead of numerical solution of (13). The simplest ansatz was proposed by Aharoni [43], where the nontrivial out–of–plane vortex structure exists inside the vortex core, when $\rho<\rho_{\mathrm{c}}$, and takes a form $\cos\theta=1-\rho^2/{\rho_{\mathrm{c}}}^2$. However, such a model does not satisfy, even approximately, Eq. (15). More realistic sounds the exchange ansatz by Usov [46]; according to the Usov ansatz the vortex out–of–plane structure takes the form of Belavin–Polyakov soliton inside the core, and, takes zero value outside:

$$m_z(\rho)=\begin{cases}\dfrac{{\rho_{\mathrm{c}}}^2-\rho^2}{{\rho_{\mathrm{c}}}^2+\rho^2}, & \text{when } \rho<\rho_{\mathrm{c}},\\ 0, & \text{when } \rho>\rho_{\mathrm{c}}.\end{cases} \quad (16)$$

In this ansatz, and some other modifications [45, 47–49], the magnetostatic energy appears only through the core radius ρ_{c}; for thin disks $\rho_{\mathrm{c}}\approx 2\ell/L$ [50]. Note that this ansatz has a singularity at $\rho=\rho_{\mathrm{c}}$. The regular model was proposed by Feldtkeller [44]. According to the Feldtkeller ansatz, the vortex out–of–plane structure has a gaussian form,

$$m_z(\rho)=\exp\left(-\frac{\rho^2}{{\rho_{\mathrm{c}}}^2}\right) \quad (17)$$

with ρ_{c} being the variational parameter. In the limit cases $\ell/L\to 0$ and $\varepsilon\to 0$, the analytical solution gives $\rho_{\mathrm{c}}=\sqrt{2}\ell/L$ [44]. The core radius slightly depends on the disk thickness, $\rho_{\mathrm{c}}\approx\sqrt{2}\ell/L\sqrt[3]{1+0.39h/\ell}$ [51].

The deviations from the easy–plane models appears due to the finite thickness of the magnet, where the structure is described by the Eq. (13). The new feature is an appearance of the magnetostatic halo, that is, the region with $\cos\theta<0$ [52]. The simplest model, which admits the appearance of halo is the Höllinger ansatz [53]

$$m_z(\rho)=C\exp(-\rho^2L^2/2\ell^2)+(1-C)\exp(-\rho^2L^2/8\ell^2). \quad (18)$$

The further generalization can be found in Ref. [40, p. 265].

To analyze the halo we have to solve Eq. (13). The problem appears with the nonlocal magnetostatic part; it can be treated using a Fourier–Bessel transform of the magnetization,

$$\hat{m}(q)=\int_0^\infty J_0(\rho q)m(\rho)\rho d\rho,\qquad m(\rho)=\int_0^\infty J_0(\rho q)\hat{m}(q)qdq. \quad (19)$$

The magnetostatic energy (12) takes a form

$$W^{\mathrm{ms}}=4\pi\int_0^\infty\hat{m}^2(q)g(2\varepsilon q)qdq,$$

where the integration limits were extended to infinity due to the local shape of $m_z(\rho)$. The local shape of $m_z(\rho)$ gives a possibility to simplify the expression (11) for the exchange energy: one can replace θ'^2 by $m_z'^2$. The second term in the energy density $\sin^2\theta/\rho^2$, which appears only due to the out–of–plane magnetization, we replace by the constrain $m_z(\rho_0)=m_0$. Thus, we can approximately write down the exchange energy in the following form:

$$W^{\mathrm{ex}}\approx\frac{4\pi\ell^2}{L^2}\int_0^\infty\left\{m_z'^2-\lambda\delta(\rho-\rho_0)[m_z(\rho)-m_0]\right\}\rho d\rho,$$

where $m(\rho)<m_0$ for $\rho>\rho_0$ and $\lambda>0$; the integration limits were extended to infinity. Using the transform (19), one can rewrite the exchange energy in the following form

$$W^{\mathrm{ex}}\approx\frac{4\pi\ell^2}{L^2}\int_0^\infty[q^2\hat{m}^2(q)-\rho_0\lambda J_0(q\rho_0)\hat{m}(q)]qdq.$$

By minimizing the total energy

$$W\approx\frac{4\pi\ell^2}{L^2}\int_0^\infty\{\hat{m}^2(q)[q^2+g(2\varepsilon q)L^2/\ell^2]-\hat{m}(q)\rho_0\lambda J_0(q\rho_0)\}qdq \quad (20)$$

with respect to $\hat{m}(q)$, one can find

$$\hat{m}(q) = \frac{\rho_0 \lambda}{2} \frac{J_0(q\rho_0)}{q^2 + g(2\varepsilon q)L^2/\ell^2}. \tag{21}$$

Using the Fourier–Bessel inversion (19) and determing the parameter λ from the constrain $m_z(\rho_0) = m_0$, one finally obtain the out–of–plane vortex structure in the following form:

$$m_z(\rho) = m_0 \frac{F(\rho)}{F(\rho_0)}, \quad F(x) = \int_0^\infty \frac{J_0(q\rho_0)J_0(qx)qdq}{q^2 + g(2\varepsilon q)L^2/\ell^2}, \tag{22}$$

where the function $g(\bullet)$ is defined in Eq. (12a).

To check different approaches, we performed two kinds of simulations. The first type is public available 3D micromagnetic OOMMF simulator [54] (developed by M. J. Donahue and D. Porter mainly from NIST. We used the 3D version of the 1.2α 2 release) with Py parameters: $A = 2.6 \times 10^{-6}$ egr/cm, $M_S = 8.6 \times 10^2$ Gs, $\alpha = 0.006$. This corresponds to the exchange length $\ell = \sqrt{A/4\pi M_S^2} \approx 5.3$ nm; the mash size is 2 nm. The second type is original spin–lattice SLASI simulator [55], based on discrete LLG equations (2) for the lattice spins, where the 3D spin distribution is supposed to be independent on z coordinate. Comparison of different approaches is plotted on Figure 1. The slight difference between two types of simulations is due to different ratio L/ℓ. One can see that only the Fourier transform model (22) describes the halo quite well (as initial parameters we used the constrain $m_z(0.1) = 0.37$ from numerical data).

3.1. GYROSCOPIC VORTEX DYNAMICS

Under the influence of external force the vortex starts to move. If such forces are weak, the vortex behaves like a particle during its evolution. Such a rigid vortex dynamics can be well–described using a Thiele approach [56, 57]. Following this approach, one can use the travelling wave ansatz (TWA):

$$\boldsymbol{m}(\boldsymbol{r}, \tau) = \boldsymbol{m}(\boldsymbol{r} - \boldsymbol{R}(\tau)), \tag{23}$$

where the vortex center position $\boldsymbol{R}(\tau)$ becomes a collective variable. By integrating the Landau–Lifshitz equations (6) with the TWA, one can calculate the effective equation of the vortex motion (Thiele equation):

$$G[\dot{\boldsymbol{R}} \times \hat{\boldsymbol{z}}] = \boldsymbol{F} - \eta \dot{\boldsymbol{R}}. \tag{24}$$

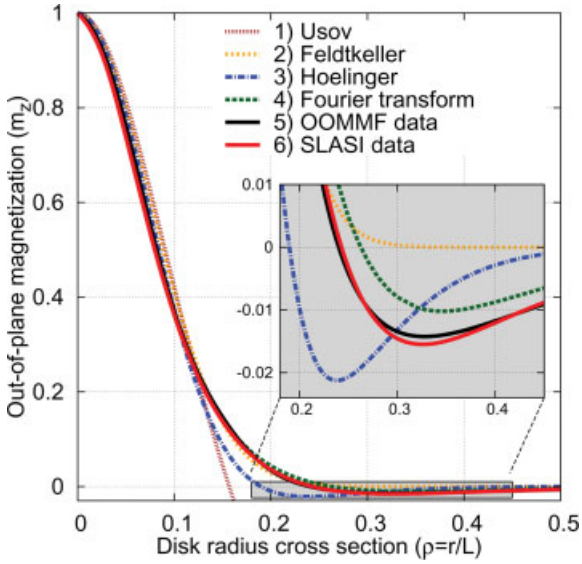

FIGURE 1. The vortex out–of–plane structure. The dashed lines corresponds to the analytical models: (1) by Usov (16), (2) by Feldtkeller (17), (3) by Höllinger (18), and (4) the Fourier–transform model (22), see details in the text. The continuous curves corresponds to the simulations data: (5) the micromagnetic OOMMF simulations for the Py disk with $2L = 200$ nm and $h = 20$ nm (aspect ratio $\varepsilon = 0.1$); (6) the discrete SLASI simulations with $2L = 100a_0$, $h = 10a_0$, $\ell = 2.65a_0$ ($\varepsilon = 0.1$). [Color figure can be viewed in the online issue, which is available at www.interscience.wiley.com.]

Here the force in the lefthandside is a gyroscopical force ($G = -4\pi Q = -2\pi p$ is the gyroconstant), which acts on a moving vortex in the same way as the Lorentz force acts on a moving charged particle in a magnetic field. The force $\boldsymbol{F} = -(1/h)\nabla_{\boldsymbol{R}}\mathscr{E}$ is external force, which comes from the total energy functional (3). The last term describes the Gilbert damping with $\eta = \pi\alpha \ln(L/\ell)$.

We obtained Thiele equations (24) using the TWA (23), which is a good approach for an infinite film. However for the finite size system, the boundary conditions should be taken into account. In a finite system with a vortex situated far from the boundary, the boundary conditions lead first of all to a modification of the in–plane magnetization. For a circular geometry and fixed (Dirichlet) boundary conditions, one can use the image vortex ansatz (IVA) [58]:

$$\cos\theta^{\mathrm{IVA}} = m_z(z - Z(t)), \tag{25a}$$

$$\phi^{\mathrm{IVA}} = \mathfrak{C}\pi/2 + \arg(z - Z(t)) + \arg(z - Z_I(t)) - \arg Z(t). \tag{25b}$$

Here $Z_I = ZL^2/R^2$ is the image vortex coordinate, which is added to satisfy the Dirichlet boundary conditions. By integrating the Landau–Lifshitz equations (6) with the IVA, we obtain formally Thiele equations in the form (24).

Let us start to calculate forces in Eq. (24) with the exchange energy contribution. By neglecting the out–of–plane vortex structure, one can calculate how the exchange energy changes due to the vortex shift. In case of the TWA model, it has the form [59]

$$\mathscr{E}^{ex} = \frac{\pi}{2} h\ell^2 \ln(1-s^2), \quad s \equiv \frac{R}{L}, \tag{26}$$

in the case of the IVA model one has

$$\mathscr{E}^{ex} = -\pi h\ell^2 \ln(1-s^2). \tag{27}$$

In the last case, the exchange energy increment is positive and for the small vortex displacements it is $\mathscr{E}^{\rm ex} \approx \pi h\ell^2 s^2$, and the restoring force $\boldsymbol{F}^{\rm ex} = -k^{\rm ex}\boldsymbol{R}$ with $k^{ex} = 2\pi(\ell/L)^2$. This force produces a vortex gyration with a frequency $\Omega^{\rm ex} = k^{\rm ex}/|G| = \ell^2/L^2$. In the case of non small vortex shifts one has [58]

$$\Omega^{\rm ex} = \frac{L^2}{|G|}\partial_s \mathscr{E}^{\rm ex} = \left(\frac{\ell}{L}\right)^2 \frac{1}{1-s^2}. \tag{28}$$

This result was obtain without the magnetostatic contribution; the last one drastically changes the picture. The stray field produces two contributions: (i) by the surface charges $\sigma^{\rm ms} = \boldsymbol{m}\cdot\boldsymbol{n}$ and (ii) by the volume charges $\lambda^{\rm ms} = -\boldsymbol{\nabla}\cdot\boldsymbol{m}$. To calculate the magnetostatic energy contribution, one has to make some assumptions about the magnetization configuration of the shifted vortex. The simplest way is to use the rigid TWA approach, where the shifted vortex produces the edge surface charges without volume charges; this leads to the rigid vortex model by Metlov [60]:

$$\mathcal{R}(z,\bar{z}) \equiv \cot(\theta/2)e^{\imath\phi} = \begin{cases} f(z), & |f(z)| < 1, \\ \sqrt{\dfrac{f(z)}{\bar{f}(z)}}, & |f(z)| \geq 1, \end{cases} \tag{29a}$$

$$f(z) = \frac{\imath(z-Z)}{\rho_c L}. \tag{29b}$$

The vortex gyration in the framework of the rigid model was calculated in Refs. [59, 61, 62]. Another model is the pole–free model by Metlov [63], which takes a form (29) with the function

$$f(z) = \frac{\imath}{\rho_c L}\left[z - \frac{1}{2}\left(Z - \bar{Z}\frac{z^2}{L^2}\right)\right]. \tag{30}$$

This model provides the fixed boundary conditions, which prevents to the appearance of edge surface charges. Hence, the magnetostatic energy of this model is caused only by the volume charges [47]. A similar and more simple model, which provides the absence of edge surface charges, is mentioned above IVA (25); below we will use namely the IVA.

A comparison of the rigid vortex and the pole–free models with simulations data has shown that the pole–free model better describes the gyroscopical vortex motion [62]. Recently, the correctness of the pole–free model was independently confirmed theoretically by the linear mode analysis [35, 64, 65, 67] and experimentally [4, 65, 66]. Results of comparison of different approaches is presented on Figure 2.

Now we are able to calculate the stray field energy of the shifted vortex. We start with the image–vortex ansatz (25). By neglecting the out–of–plane contribution of the vortex structure, one can calculate the magnetostatic charges as follows:

$$\lambda^{\rm ms}(\boldsymbol{r}) = \frac{2\mathfrak{C}s}{L}\Lambda(r/L, s, \chi), \tag{31a}$$

where the function $\Lambda(\xi, s, \chi)$ takes the following form:

$$\Lambda(\xi,s,\chi) = \frac{\xi\sin\chi}{\sqrt{s^2+\xi^2-2s\xi\cos\chi}\sqrt{1+s^2\xi^2-2s\xi\cos\chi}}. \tag{31b}$$

Here the origin of normalized polar coordinate frame ($\xi \equiv r/L, \chi$) coincides with disk center and angle χ is counted from the direction of the shifted vortex. Then the normalized magnetostatic vortex energy (5b) reads

$$\mathscr{E}^{\rm ms} = \frac{1}{8\pi}\int d\boldsymbol{r}\int d\boldsymbol{r}'\frac{\lambda^{\rm ms}(\boldsymbol{r})\lambda^{\rm ms}(\boldsymbol{r}')}{|\boldsymbol{r}-\boldsymbol{r}'|} = \pi s^2 h^2 L\,\Xi(\varepsilon, s), \tag{32a}$$

$$\Xi(\varepsilon,s) = \frac{1}{\pi^2}\int_0^1 d\zeta\int_0^1 d\xi\int_0^1 d\xi'\int_0^{2\pi} d\chi \times \int_0^{2\pi} d\psi \frac{\xi\xi'(1-\zeta)\Lambda(\xi,s,\chi)\Lambda(\xi',s,\chi+\psi)}{\sqrt{\xi^2+\xi'^2-2\xi\xi'\cos\psi+4\varepsilon^2\zeta^2}}. \tag{32b}$$

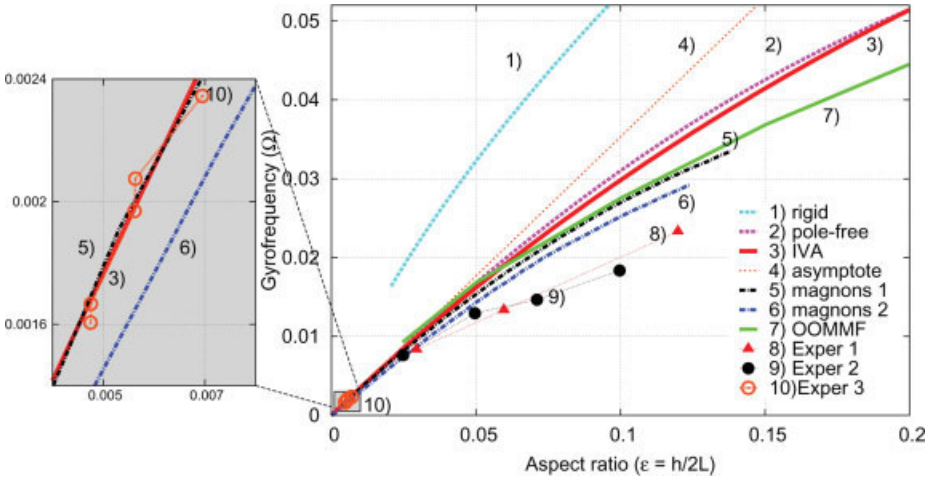

FIGURE 2. The vortex gyrofrequency Ω depending on the disk aspect ratio $\varepsilon = h/2L$. The dashed lines corresponds to the Metlov's ansatz following Ref. [62]: the curve (1) corresponds to the rigid ansatz (29), the curve (2) to the pole–free ansatz (30). The continuous line (3) is the theoretical calculation (34) using the image vortex ansatz. The dotted line (4) is the asymptote (35). The dashed–dotted line (5) is the magnon mode frequency according to Ref. [64], (6) the same by Ref. [65]. The continuous line (7) is the OOMMF simulations data. The symbols (8) are the experimental data, see Ref. [4], symbols (9) are the experimental data by Ref. [65]. Symbols (10) corresponds to the experimental data by Ref. [66]. [Color figure can be viewed in the online issue, which is available at www.interscience.wiley.com.]

Let us start with the case of small vortex displacements ($s \to 0$) and limit ourselves by the limit case of $\Xi(\varepsilon, 0)$. The last one takes a know form [47]

$$\Xi(\varepsilon,0) = \int_0^\infty dx \mathfrak{g}(\varepsilon,x)\left[\int_0^1 \xi d\xi J_1(x\xi)\right]^2,$$

$$\mathfrak{g}(\varepsilon,x) = \frac{2\varepsilon x - 1 + e^{-2\varepsilon x}}{2x^2\varepsilon^2}. \quad (33)$$

One can see that for small vortex displacements the energy has the harmonic law $\mathscr{E}^{\rm ms} = khR^2/2$, and the restoring force $\boldsymbol{F}^{\rm ms} = -k\boldsymbol{R}$ with $k = 4\pi\varepsilon\Xi(\varepsilon,0)$. Therefore, the Thiele equation (24) results in a vortex gyration, where the vortex precess with the frequency

$$\Omega(\varepsilon) = \frac{k}{|G|} = 2\varepsilon\Xi(\varepsilon,0). \quad (34)$$

This frequency corresponds to the frequency of the gyrotropic magnon mode on a vortex, which lies typically in a sub-GHz range [62, 64, 66–68]. The dependence (34) is plotted by the curve (3) on Figure 2; it agrees well with experimental and simulations data.

In the case of very thin films ($\varepsilon \to 0$), all calculations can be done analytically, see Appendix: the gyrofrequency

$$\Omega_0 = 2\varepsilon\Xi(0,0) = \frac{4\varepsilon}{3\pi}(2\mathfrak{G} - 1) \approx 0.3531\varepsilon, \quad (35)$$

which is in a good agreement with the result [66]: $\Omega_0 \approx 10\varepsilon/(9\pi) \approx 0.3537\varepsilon$.

In the case of a nonsmall vortex displacement, one can use the general expression (32), which leads to the gyrofrequency

$$\Omega(\varepsilon,s) = 2\varepsilon\left[\Xi(\varepsilon,s) + \frac{s}{2}\partial_s\Xi(\varepsilon,s)\right]. \quad (36)$$

Now, using $\Xi(\varepsilon,s)$ from Eq. (32b), one can calculate the gyrofrequency in a wide range of aspect ratios and the vortex shifts, see Figure 3. In the limit case of thin disks, $\varepsilon \to 0$, the numerical data can be fitted (with the accuracy 1.2% in the range $s \in (0; 0.5)$) by the dependence,

$$\Omega(\varepsilon \to 0, s) \approx \frac{4\varepsilon}{3\pi}\frac{2\mathfrak{G} - 1}{1 - (s/2)^2}. \quad (37)$$

In order to check dependencies $\Omega(\varepsilon,s)$, we performed SLASI simulations, see Figure 3. Our analytical calculations correspond to the simulation data quite well for $s < 0.5$. For the higher vortex shift, the model image–vortex ansatz does not work, because the vortex out–of–plane structure is deformed. We will see below in Section that such deformation can even switch the vortex magnetization.

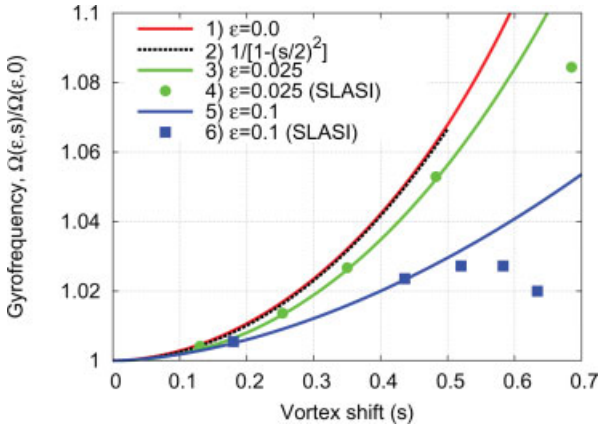

FIGURE 3. The vortex gyrofrequency $\Omega(\varepsilon, s)$ normalized by $\Omega(\varepsilon, 0)$ as a function of the vortex shift $s \equiv R/L$. The continuous line (1) corresponds to analytical caluclations by (36), (32b) for $\varepsilon = 0$, the dashed curve (2) is the approximate dependence (37). The continuous curves (3) and (5) correspond to calculations for $\varepsilon = 0.025$ and $\varepsilon = 0.1$, respectively. Symbols are the SLASI simulations data: (4) correspond to $\varepsilon = 0.025$ for the spin lattice $2L = 40a_0$, $h = a_0$, and $\ell = 1.4a_0$; symbols (5) correspond to $\varepsilon = 0.1$, $2L = 50a_0$, $h = 5a_0$, and $\ell = 1.3a_0$. [Color figure can be viewed in the online issue, which is available at www.interscience.wiley.com.]

4. Current driven vortex dynamics

Let us discuss the effects of an electrical current on the vortex dynamics in magnets. As we discussed in the introduction, the current influences the spin dynamics of the magnet due to the spin–torque effect. There exist two main kinds of heterostructures, where the spin-torque effect is observed [8]: a current-in-plane (CIP) structure, where both polarizer and sensor layer are magnetized in plane and a current-perpendicular-to-the-plane (CPP) structure, where the sensor is in-plane magnetized, while the polarizer is magnetized perpendicular to the plane. We consider the CPP heterostructure with a vortex state sensor, which was proposed recently in Refs. 37, 38.

It is well–known [12] that the spin torque effect causes a spin precession in a homogeneously magnetized particle. A similar picture also takes place for the vortex state Heisenberg system [37], where the spin current, which is perpendicular to the nanoparticle plane, mainly acts like an effective perpendicular DC magnetic field. Recently, we have shown [38] that the dipolar interaction crucially changes the physical picture of the process. The precessional vortex state [37] becomes unfavorable, because the dipolar interaction tries to minimize the edge surface magnetostatic charges, hence the magnetization at the dot edge is almost conserved [67].

We consider a pillar structure [37, 69, 70], in which the magnetization direction in the polarizer is aligned parallel to z (see Fig. 4). An electrical current is injected in the polarizer, where it is polarized along the unit vector $\boldsymbol{\sigma}$ (which is collinear to z in our case). The sensor is a thin disk with a vortex ground state: the magnetization lies in the disk plane in the main part of the disk being parallel to the disk edge; however in the disk center, the magnetization becomes perpendicular to the disk plane in order to prevent a singularity in the magnetization distribution [40, 58]. This perpendicular magnetization distribution forms the vortex core, which is oriented along z or opposite to z. Such a direction of the core magnetization is characterized by the vortex polarity ($p = +1$ or $p = -1$, respectively). In the pillar stack, the thickness of the nonmagnetic layer (spacer) is much less than the spin diffusion length [69, 71], hence the spin polarization of the current is conserved when it flows into the sensor.

The spin dynamics can be described by the LLG spin–lattice equations (2) with an additional spin–torque term $\boldsymbol{T}_n$ in the right hand side [12, 13] of the following form:

$$\boldsymbol{T}_n = \frac{j\mathcal{A}\omega_0}{S + \mathcal{B}\boldsymbol{S}_n \cdot \boldsymbol{\sigma}} [\boldsymbol{S}_n \times [\boldsymbol{S}_n \times \boldsymbol{\sigma}]], \tag{38}$$

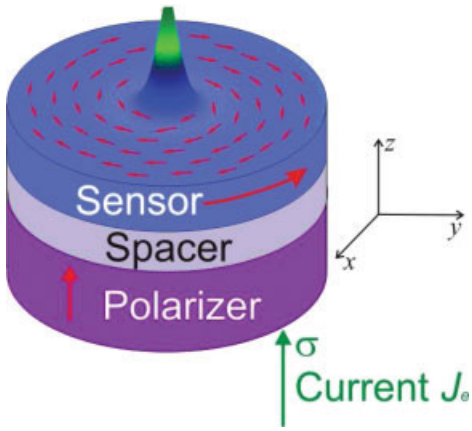

FIGURE 4. Schematic of the CPP heterostructure used for the current induced vortex dynamics. [Color figure can be viewed in the online issue, which is available at www.interscience.wiley.com.]

$$\mathcal{A}=\frac{4\eta_{sp}^{3/2}}{3(1+\eta_{\rm sp})^3-16\eta_{\rm sp}^{3/2}},\quad \mathcal{B}=\frac{(1+\eta_{\rm sp})^3}{3(1+\eta_{\rm sp})^3-16\eta_{\rm sp}^{3/2}}. \tag{39}$$

Here $j=J_{\rm e}/J_p$ is a normalized spin current, J_e being the electrical current density, $J_{\rm p}=M_{\rm S}^2|e|h/\hbar$, e being the electron charge, and $\eta_{\rm sp}\in(0;1)$ being the degree of the spin polarization.

In the continuous limit one can use the LLG Eqs. (40) with an additional spin–torque term:

$$\sin\theta\partial_\tau\phi=-\frac{\delta\mathscr{E}}{\delta\theta}-\alpha\partial_\tau\theta, \tag{40a}$$

$$-\sin\theta\partial_\tau\theta=-\frac{\delta\mathscr{E}}{\delta\phi}-\alpha\sin^2\theta\partial_\tau\phi+\frac{\varkappa\sin^2\theta}{1+\mathcal{B}\sigma\cos\theta}, \tag{40b}$$

where we introduced the normalized current $\varkappa=j\sigma\mathcal{A}$. We are interested here by the influence of the homogeneous spin torque $T\propto \boldsymbol{j}\cdot\boldsymbol{m}$ only. Note that such an approach is adequate if the magnetization does not change in the direction of the current propagation ($\ell|\partial_z\boldsymbol{m}|\ll 1$); this is reasonable for the perpendicular current and thin nanodisks. However, if one applies a current in the direction of the disk plane, there appears a nonhomogeneous spin torque $T\propto(\boldsymbol{j}\cdot\nabla)\boldsymbol{m}$ [72], which causes another mechanism of the vortex dynamics [32, 34, 39, 73, 74].

We start to analyze the spin torque effect with a quasi–uniform ground state, which is the in–plane magnetized disk. Under the influence of the spin current, the homogeneous ground state of the system changes: there appears a dynamical cone state with the out-of-plane magnetization,

$$\cos\theta_{\rm h}=\frac{\sigma}{2\mathcal{B}}(\sqrt{1+4\varkappa\mathcal{B}\sigma/\alpha}-1)\approx\frac{\varkappa}{\alpha},\qquad \Omega_{\rm h}\equiv\partial_\tau\phi=\cos\theta_{\rm h}, \tag{41}$$

where the in–plane magnetization angle ϕ rotates around z–axes with a frequency $\Omega_{\rm h}$. This state is stable only for $|\varkappa-\alpha\mathcal{B}|<\alpha$. Together with this state there is always the fixed point $\theta_{\rm h}=0$ (resp. $\theta_{\rm h}=\pi$), which is stable for $\varkappa-\alpha\mathcal{B}>\alpha$ (resp. $\varkappa-\alpha\mathcal{B}>-\alpha$).

Let us discuss the vortex state nanodisk and study the influence of the spin–torque effect in the vortex dynamics. The standard way to derive the effective equations of motions one can multiply Eq. (40a) by $\nabla\theta$, Eq. (40b) by $\nabla\phi$, to add results and to integrate it by the sample volume. By incorporating the image–vortex ansatz (25) into this force balance equation, one can finally obtain, similar to the Thiele equation (24):

$$G[\boldsymbol{e}_z\times\dot{\boldsymbol{R}}]-2\pi\eta\dot{\boldsymbol{R}}-2\pi\Omega(\varepsilon,s)\boldsymbol{R}+\boldsymbol{F}^{\rm ST}=0. \tag{42a}$$

The last term in the right hand side, $\boldsymbol{F}^{\rm ST}$, is a spin–torque force:

$$\boldsymbol{F}^{\rm ST}=-\varkappa\int d^2x\frac{\sin^2\theta}{1+\mathcal{B}\sigma\cos\theta}\nabla\phi. \tag{42b}$$

To treat this force analytically, we can neglect the $\mathcal{B}$–term in denominator. Using the ansatz (25), one can approximately calculate $\boldsymbol{F}^{\rm ST}$ in the form [35, 36, 75]:

$$\boldsymbol{F}^{\rm ST}\approx-\varkappa\int d^2x\nabla\phi=-\pi\varkappa q[\boldsymbol{R}\times\boldsymbol{e}_z]. \tag{42c}$$

Using the polar coordinates for the vortex position, $Z=(X+\imath Y)=Re^{\imath\Phi}$, one can rewrite (42) in the following form:

$$\dot\Phi=p\Omega(\varepsilon,s)-2\pi\eta\frac{\dot R}{R},\quad \frac{\dot R}{R}=-\eta p\dot\Phi-\frac{1}{2}\varkappa p. \tag{43}$$

Without the spin current term, the vortex stays at the disk center, which is a ground state. This stability of the origin is provided by the damping. However, the loss of energy due to the damping can be compensated by the energy pumping due to the spin current if the current exceeds a critical value, see below. One can see from Eq. (43) that the vortex position at origin can be unstable when $p\varkappa<0$. The spin current excites a spiral vortex motion, which finally leads to the circular limit cycle $Z(\tau)=R_0\exp(\imath\omega\tau)$ with the frequency

$$\omega=p\Omega(\varepsilon,s_0)=-\frac{\varkappa}{2\eta}. \tag{44}$$

The critical current can be easily estimated as follows:

$$\varkappa_{\rm cr}=2\eta\Omega(\varepsilon),\quad j_{\rm cr}=\frac{2\eta\Omega(\varepsilon)}{\mathcal{A}}, \tag{45}$$

where $\Omega(\varepsilon)=\Omega(\varepsilon,s=0)$, see (34). The spiral vortex motion can be excited under the conditions: $|j|>j_{\rm cr}$ and $pj\sigma<0$. Note that for small aspect ratios $\varepsilon\equiv h/2L\ll 1$, one can use the approximation $\Omega(\varepsilon)\approx\Omega_0=4\varepsilon(2\mathfrak{G}-1)/(3\pi)$, see (35), hence,

$$j_{\rm cr}\approx\frac{4\alpha h(2\mathfrak{G}-1)}{3\mathcal{A}L}\ln\frac{L}{\ell}. \tag{46}$$

The radius of the limit cycle $R_0 = Ls_0$ can be found by solving the equation

$$\frac{\Omega(\varepsilon, s_0)}{\Omega(\varepsilon)} = \frac{|j|}{j_{\rm cr}}. \tag{47}$$

In the limit case of infinitesimally thin disks one can use the approximate dependence (37), which leads to the limit cycle radius as follows,

$$R_0 = 2L\sqrt{1 - \frac{j_{\rm cr}}{|j|}}. \tag{48}$$

Note that similar threshold dependence was obtained recently in Ref. [35], $R_0 = 0.153L\sqrt{(j - j_{\rm c})/j_{\rm c}}$. Very recently, the existence of the limit cycle by the spin current was confirmed experimentally [36].

To check analytical results, we performed numerical simulations of the discrete spin–lattice LLG equations (2) with additional spin–torque term in the form (38). In simulation's we observed that the vortex does not quit the disk center, which is a stable point, if we apply the current, whose polarization is parallel to the vortex polarity ($j\sigma p > 0$). However, if the spin current has the opposite direction of the spin polarization ($j\sigma p < 0$, $p = +1$, $\sigma = +1$, and $j < 0$ in our case), the vortex motion can be excited when the current intensity is above a threshold value [35, 75, 76] as a result of the balance between the pumping and damping. Following the spiral trajectory, the vortex finally reaches a circular limit cycle. The rotation sense of the spiral is determined by the gyroforce, that is, by the topological charge Q [see (10)], which is a clockwise rotation in our case. The vortex motion can be excited only if the current strength exceeds some critical value $j_{\rm cr}$, see Figure 5. Numerically we found that $j_{\rm cr} = 0.0165$, which corresponds to $\varkappa_{\rm cr} = 7.94 \times 10^{-4}$. This result is in a good agreement with $\varkappa_{\rm cr} = 7.96 \times 10^{-4}$, which we obtained using (45).

The radius of the vortex trajectory increases with a current intensity in accordance to (48). At some value, the radius becomes comparable with the system size L and the vortex dynamics becomes nonlocal: it cannot be described by the Eq. (24). Finally, it results in a switching of the vortex core.

The switching process is detailed on Figure 6. The mechanism of the vortex switching is essentially the same in all systems where the switching was observed [32, 38, 75, 77–81]. Under the action of the spin current, the vortex ($q_{\rm V} = +1, p_{\rm V} = +1$, $Q_{\rm V} = +1/2$), originally situated in the disk center, see

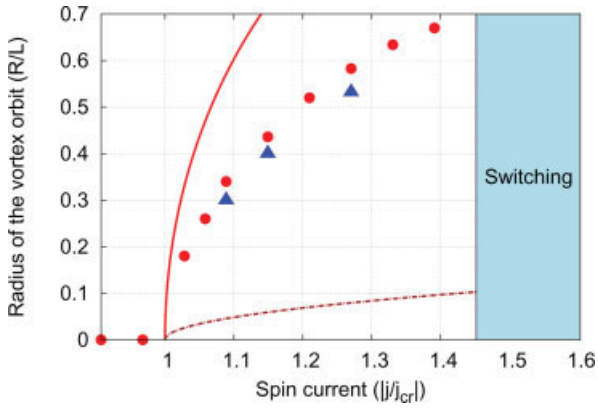

FIGURE 5. Limit cycle for different currents. Symbols corresponds to simulations data: • for the original system and ▲ for the simplified one with $\mathscr{B} = 0$; the solid curve is the analytical dependence (48); the dashed curve is the analytical result from Ref. [35]. Simulations parameters: $2L = 50a_0$, $h = 5a_0$, $\ell = 1.3a_0$, $\alpha = 0.01$, $\sigma = -1$, $\eta_{\rm sp} = 0.26$. [Color figure can be viewed in the online issue, which is available at www.interscience.wiley.com.]

Figure 6(a), starts to move along the spiral trajectory, in the clockwise direction in our case, see Figure 7(a). The moving vortex excites an azimuthal magnon mode with a dip situated towards the disk center, see Figure 6(b). When the vortex moves away from the center, the amplitude of the dip increases, see Figure 6(c). When the amplitude of the out-of-plane dip reaches its minimum [$m_z = -1$, Fig. 6(c)] a pair of a new vortex (NV, $q_{\rm NV} = +1, p_{\rm NV} = -1, Q_{\rm NV} = -1/2$) and antivortex (AV, $q_{\rm AV} = -1, p_{\rm AV} = -1, Q_{\rm AV} = +1/2$) is created. These three objects move following complicated trajectories which result from Thiele–like equations. The directions of the motion of the partners are determined by the competition between the gyroscopical motion and the external forces, which are magnetostatic force $F^{\rm ms}$, pumping force $F^{\rm ST}$, see Eqs. (42), and the interactions between the vortices $\boldsymbol{F}_i^{\rm int}$. The reason why the new-born vortex tears off his partner has a topological origin. The gyroscopic force depends on the total topological charge Q. Therefore, it produces a clockwise motion for the original vortex and the new-born antivortex, while the new-born vortex moves in the counterclockwise direction. As a result, the new vortex separates from the vortex-antivortex pair and rapidly moves to the origin, see Figures 6(d) and 7(a). The attractive force between the original vortex ($q = 1$) and the antivortex ($q = -1$) facilitates a binding and subsequent annihilation of the vortex-antivortex pair, see Figure 6(e).

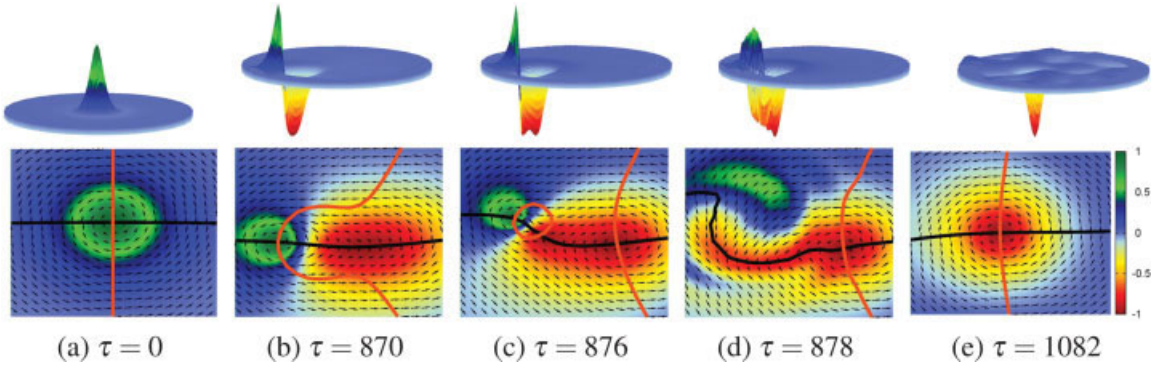

FIGURE 6. The temporal evolution of the vortex during the switching process by SLASI simulations: the upper row corresponds to the distribution of S^z spin components, the lower row corresponds to the in–plane spins around the vortex core. Isosurfaces $S_x = 0$ (black curve) and $S_y = 0$ (orange curve) are plotted to determine positions of vortices and the antivortex. The simulation parameters: $2L = 100a_0$, $h = 10a_0$, $\ell = 2.65a_0$, $\alpha = 0.01$, $\sigma = +1$, $\eta_{sp} = 0.26$, $j = -0.1$. [Color figure can be viewed in the online issue, which is available at www.interscience.wiley.com.]

The three–body process for the Heisenberg magnets in a no-driving case is studied in details in Ref. [82]. The internal gyroforces of the dip impart the initial velocities to the NV and AV, which are perpendicular to the initial dip velocity and have opposite directions. In this way, the AV gains the velocity component directed to the center, where the V is moving. This new-born pair is a topologically trivial $Q = 0$ pair, which undergoes a Kelvin motion [83]. This Kelvin pair collides with the original vortex. If the pair was born far from V then the scattering process is semi–elastic; the new-born pair is not destroyed by the collision. In the exchange approach, this pair survives, but it is scattered by some angle [84]. Because of the additional forces (pumping, damping, and magnetostatic interaction), the real motion is more complicated and the Kevin pair can finally annihilate by itself. Another collision mechanism takes place when the pair is born closer to the original vortex. Then the AV can be captured by the V and an annihilation with the original vortex happens. The collision process is essentially inelastic. During the collision, the original vortex and the antivortex form a topological

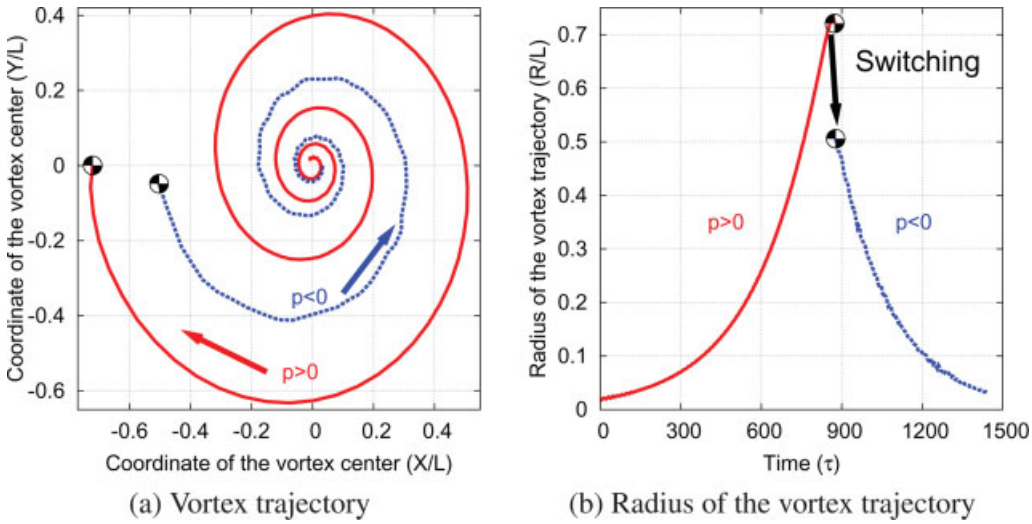

FIGURE 7. The vortex dynamics under the switching by SLASI simulations for $j = -0.1$. Continuous curve corresponds to the vortex trajectory before switching ($p > 0$), the dashed curve corresponds to the vortex trajectory after the switching ($p < 0$); at $\tau = 877$ the vortex polarity is switched. [Color figure can be viewed in the online issue, which is available at www.interscience.wiley.com.]

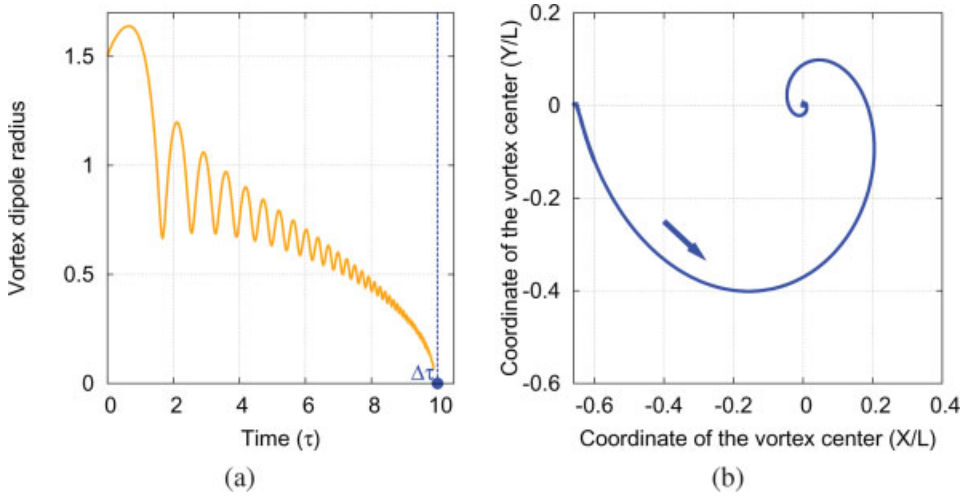

FIGURE 8. Numerical solution of Eq. (50) for the system with $2L = 100a_0$, $\ell = 2.65a_0$, $\alpha = 0.01$, $\varkappa = -0.027$, $\Omega = 0.0287$. The original vortex was situated at $(-36a_0, 0)$, the antivortex at $(-34.5a_0, 0)$, and the new-born vortex at $(-33a_0, 0)$: (a) the distance between the original vortex and the antivortex (vortex dipole radius $R_{\text{dipole}} = |\boldsymbol{R}_{\text{V}} - \boldsymbol{R}_{\text{AV}}|$) as a function of dimensionless time τ; (b) the trajectory of the new-born vortex. [Color figure can be viewed in the online issue, which is available at www.interscience.wiley.com.]

nontrivial pair ($Q = +1$), which performs a rotational motion around some guiding center [84, 85]. This rotating vortex dipole forms a localized skyrmion (Belavin-Polyakov soliton [86]), which is stable in the continuum system. In the discrete lattice system, the radius of this soliton, that is, the distance between vortex and antivortex, rapidly decreases almost without energy loss. When the soliton radius is about one lattice constant, the pair undergoes the topologically forbidden annihilation [81, 85], which is accompanied by strong spin-wave radiation, because the topological properties of the system change [87, 88].

Let us describe the three-body system with account of the megnetostatic interaction and the spin-torque driving. The magnetostatic force for the three body system can be calculated, using the image vortex approach, which corresponds to fixed boundary conditions. For the vortex state, nanodisk such boundary conditions results from the magnetostatic interaction, which is localized near the disk edge [67]. The same statement is also valid for the three vortex (V-AV-NV) state, which is confirmed also by our numerical simulations. The ϕ–field can be presented by the three vortex ansatz,

$$\phi = \sum_{i=1}^{3} q_i \left\{ \arg[\zeta - Z_i] + \arg\left[\zeta - Z_i^I\right] - \arg Z_i \right\} + \mathfrak{C}\frac{\pi}{2}. \tag{49}$$

Note that Ansatz (49) can be generalized for the case of N vortices and N-1 antivortices. The force coming from the volume magnetostatic charge density can be calculated in the same way as for a single vortex made above, which results in $\boldsymbol{F}_i^{\text{ms}} \approx -2\pi\Omega_G q_i \sum_j q_j \boldsymbol{R}_j$, where $q_i = \pm 1$ is the vorticity of i-th vortex (antivortex). The interaction force $\boldsymbol{F}^{\text{int}}$ between vortices is a 2D coulomb force $\boldsymbol{F}_i^{\text{int}} = 2\pi\ell^2 q_i \sum_{j\neq i} q_j \frac{\boldsymbol{R}_i - \boldsymbol{R}_j}{|\boldsymbol{R}_i - \boldsymbol{R}_j|^2}$. Finally, the three–body problem can be described by the Thiele–like equations:

$$-2Q_i[\boldsymbol{e}_z \times \dot{\boldsymbol{R}}] - \eta\dot{\boldsymbol{R}} - \Omega(\varepsilon, s) q_i \sum_j q_j \boldsymbol{R}_j + \ell^2 q_i \sum_{j\neq i} q_j \frac{\boldsymbol{R}_i - \boldsymbol{R}_j}{|\boldsymbol{R}_i - \boldsymbol{R}_j|^2} + \frac{\boldsymbol{F}_i^{\text{ST}}}{2\pi} = 0. \tag{50}$$

The set of Eq. (50) describes the main features of the observed three–body dynamics. During the evolution, the original vortex and the antivortex create a rotating dipole, in agreement with Refs. 84, 85, see Figure 8(a). The distance in this vortex dipole rapidly tends to zero. The new–born vortex moves on a counterclockwise spiral to the origin in agreement with our numerical data, see Figure 8(b).

The switching process has a threshold behavior. It occurs when the current $|j| > j_{\text{sw}}$, which is about 0.0102 in our simulations, see Figure 9. For stronger currents, the switching time rapidly decreases. Using typical parameters for permalloy

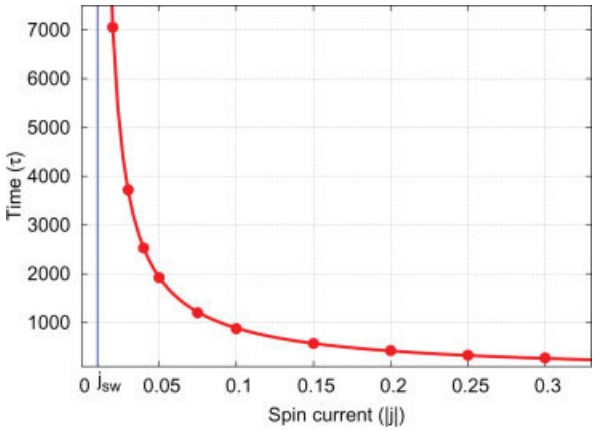

FIGURE 9. Switching time as a function of the applied current. [Color figure can be viewed in the online issue, which is available at www.interscience.wiley.com.]

disks [37, 81] ($A = 26$ pJ/m, $M_S = 860$ kA/m, $\alpha = 0.01$), we estimate that the time unit $2\pi/\omega_0 = 33$ ps, the switching current density is about 0.1 A/μm^2 for $\eta_{sp} = 0.26$ and 20 nm of a nanodot thickness. The total current for a disk with diameter 200 nm is about 10 mA.

5. Summary

As a summary, we have studied the magnetic vortex dynamics under the action of an electrical current. The steady-state vortex motion (circular limit cycle) can be excited due spin–transfer effect above a threshold current. This limit cycle results from the balance of forces between the pumping (due to the spin-torque effect) and damping (due to the Gilbert relaxation) [35, 75]. Recently, current-driven subgigahertz oscillations in point contacts caused by the large-amplitude vortex dynamics were observed experimentally [36]. In particular, it was observed a stable circular orbit outside of the contact region.

The switching of the vortex polarity takes place for a stringer current. It is important to stress that such a switching picture involving the creation and annihilation of a vortex-antivortex pair seems to be very general and does not depend on the details how the vortex dynamics was excited. In particular, such a switching mechanism can be induced by a field pulse [77–79], by an AC oscillating [80] or rotating field [81], by an in-plane electrical current (nonhomogeneous spin torque) [32, 74], and by a perpendicular current (our case, the homogeneous spin torque) [35, 38, 75]. Our analytical analysis is confirmed by numerical spin-lattice simulations.

Appendix

Let us calculate the gyrofrequency for the very thin disk. We start from the Eq. (33). In the limit case $\varepsilon \to 0$ one can write down:

$$\Xi(0,0) = \int_0^\infty dk \left[\int_0^1 \xi d\xi J_1(k\xi) \right]^2, \qquad \text{(A1)}$$

where the relation $\lim_{\varepsilon \to 0} \mathfrak{g}(\varepsilon, k) = 1$ was used. Taking into account that

$$\int_0^\infty J_1(\xi x) J_1(\xi' x)\, dx = \begin{cases} \dfrac{2}{\pi \xi'} [\mathrm{K}(\xi'/\xi) - \mathrm{E}(\xi'/\xi)], & \xi' < \xi \\ \dfrac{2}{\pi \xi} [\mathrm{K}(\xi/\xi') - \mathrm{E}(\xi/\xi')], & \xi' > \xi, \end{cases}$$

where $K(x)$ and $E(x)$ are elliptic integrals of the first and second kinds respectively, it is easy to obtain $\Xi(0,0) = \frac{4}{3\pi} \int_0^1 [\mathrm{K}(x) - \mathrm{E}(x)] dx$. After integration by parts, where the property $\frac{d}{dx} E(x) = [\mathrm{E}(x) - \mathrm{K}(x)]/x$ should be used, one can obtain the result $\Xi(0,0) = \frac{2}{3\pi}(2\mathfrak{G} - 1)$, with $\mathfrak{G} = \frac{1}{2} \int_0^1 \mathrm{K}(x) dx \approx 0.916$ being the Catalan constant [89]. The corresponding gyrofrequency takes the form (35).

References

1. Guslienko, K. Y.; Novosad, V.; Otani, Y.; Shima, H.; Fukamichi, K. Phys Rev B 2001, 65, 024414.
2. Demokritov, S. O.; Hillebrands, B.; Slavin, A. N. Phys Reports 2001, 348, 441.
3. Hillebrands, B.; Ounadjela, K. (Eds.) Spin Dynamics in Confined Magnetic Structures I, Topics in Applied Physics; Springer: Berlin, 2002; vol. 83.
4. Park, J. P.; Eames, P.; Engebretson, D. M.; Berezovsky, J.; Crowell, P. A. Phys Rev B 2003, 67, 020403.
5. Buess, M.; Hőllinger, R.; Haug, T.; Perzlmaier, K.; Pescia, U. K. D.; Scheinfein, M. R.; Weiss, D.; Back, C. H. Phys Rev Lett 2004, 93, 077207.
6. Choe, S. B.; Acremann, Y.; Scholl, A.; Bauer, A.; Doran, A.; Stohr, J.; Padmore, H. A. Science 2004, 304, 420.
7. Thirion, C.; Wernsdofer, W.; Mailly, D. Nat Mater 2003, 2, 524.
8. Zutic, I.; Fabian, J.; Sarma, S. D. Rev Mod Phys 2004, 76, 323.
9. Marrows, C. H. Adv Phys 2005, 54, 585.
10. Tserkovnyak, Y.; Brataas, A.; Bauer, G. E. W.; Halperin, B. I. Rev Mod Phys 2005, 77, 1375.

11. Bader, S. D. Rev Mod Phys 2006, 78, 1.
12. Slonczewski, J. C. J Magn Magn Mater 1996, 159, L1.
13. Berger, L. Phys Rev B 1996, 54, 9353.
14. Tsoi, M.; Jansen, A. G. M.; Bass, J.; Chiang, W. C.; Seck, M.; Tsoi, V.; Wyder, P. Phys Rev Lett 1998, 80, 4281.
15. Myers, E. B.; Ralph, D. C.; Katine, J. A.; Louie, R. N.; Buhrman, R. A. Science 1999, 285, 867.
16. Koo, H.; Krafft, C.; Gomez, R. D. Appl Phys Lett 2002, 81, 862.
17. Kiselev, S. I.; Sankey, J. C.; Krivorotov, I. N.; Emley, N. C.; Schoelkopf, R. J.; Buhrman, R. A.; Ralph, D. C. Nature 2003, 425, 380.
18. Rippard, W. H.; Pufall, M. R.; Kaka, S.; Russek, S. E.; Silva, T. J. Phys Rev Lett 2004, 92, 027201.
19. Yamaguchi, A.; Ono, T.; Nasu, S.; Miyake, K.; Mibu, K.; Shinjo, T. Phys Rev Lett 2004, 92, 077205.
20. Krivorotov, I. N.; Emley, N. C.; Sankey, J. C.; Kiselev, S. I.; Ralph, D. C.; Buhrman, R. A. Science 2005, 307, 228.
21. Tulapurkar, A. A.; Suzuki, Y.; Fukushima, A.; Kubota, H.; Maehara, H.; Tsunekawa, K.; Djayaprawira, D. D.; Watanabe, N.; Yuasa, S. Nature 2005, 438, 339.
22. Özyilmaz, B.; Kent, A. D. Appl Phys Lett 2006, 88, 162506.
23. Acremann, Y.; Strachan, J. P.; Chembrolu, V.; Andrews, S. D.; Tyliszczak, T.; Katine, J. A.; Carey, M. J.; Clemens, B. M.; Siegmann, H. C.; Stohr, J. Phys Rev Lett 2006, 96, 217202.
24. Emley, N. C.; Krivorotov, I. N.; Ozatay, O.; Garcia, A. G. F.; Sankey, J. C.; Ralph, D. C.; Buhrman, R. A. Phys Rev Lett 2006, 96, 247204.
25. Ishida, T.; Kimura, T.; Otani, Y. Phys Rev B 2006, 74, 014424.
26. Jubert, P. O.; Klaui, M.; Bischof, A.; Rudiger, U.; Allenspach, R. J Appl Phys 2006, 99, 08G523.
27. Kläui, M.; Laufenberg, M.; Heyne, L.; Backes, D.; Rudiger, U.; Vaz, C. A. F.; Bland, J. A. C.; Heyderman, L. J.; Cherifi, S.; Locatelli, A.; Mentes, T. O.; Aballe, L. Appl Phys Lett 2006, 88, 232507.
28. Ozatay, O.; Emley, N. C.; Braganca, P. M.; Garcia, A. G. F.; Fuchs, G. D.; Krivorotov, I. N.; Buhrman, R. A.; Ralph, D. C. Appl Phys Lett 2006, 88, 202502.
29. Urazhdin, S.; Chien, C. L.; Guslienko, K. Y.; Novozhilova, L. Phys Rev B 2006, 73, 054416.
30. Houssameddine, D.; Ebels, U.; Delaet, B.; Rodmacq, B.; Firastrau, I.; Ponthenier, F.; Brunet, M.; Thirion, C.; Michel, J. P.; Prejbeanu-Buda, L.; Cyrille, M. C.; Redon, O.; Dieny, B. Nat Mater 2007, 6, 447.
31. Pribiag, V. S.; Krivorotov, I. N.; Fuchs, G. D.; Braganca, P. M.; Ozatay, O.; Sankey, J. C.; Ralph, D. C.; Buhrman, R. A. Nat Phys 2007, 3, 498.
32. Yamada, K.; Kasai, S.; Nakatani, Y.; Kobayashi, K.; Kohno, H.; Thiaville, A.; Ono, T. Nat Mater 2007, 6, 270.
33. Bolte, M.; Meier, G.; Krüger, B.; Drews, A.; Eiselt, R.; Bocklage, L.; Bohlens, S.; Tyliszczak, T.; Vansteenkiste, A.; Waeyenberge, B. V.; Chou, K. W.; Puzic, A.; Stoll, H. Phys Rev Lett 2008, 100, 176601.
34. Kasai, S.; Nakatani, Y.; Kobayashi, K.; Kohno, H.; Ono, T. Phys Rev Lett 2006, 97, 107204.
35. Ivanov, B. A.; Zaspel, C. E. Phys Rev Lett 2007, 99, 247208.
36. Mistral, Q.; van Kampen, M.; Hrkac, G.; Kim, J. V.; Devolder, T.; Crozat, P.; Chappert, C.; Lagae, L.; Schrefl, T. Phys Rev Lett 2008, 100, 257201.
37. Caputo, J. G.; Gaididei, Y.; Mertens, F. G.; Sheka, D. D. Phys Rev Lett 2007, 98, 056604.
38. Sheka, D. D.; Gaididei, Y.; Mertens, F. G. Appl Phys Lett 2007, 91, 082509.
39. Cowburn, R. P. Nat Mater 2007, 6, 255.
40. Hubert, A.; Schäfer, R. Magnetic Domains: The Analysis of Magnetic Microstructures; Springer–Verlag: Berlin, 1998.
41. Stöhr, J.; Siegmann, H. C. Magnetism: From Fundamentals to Nanoscale Dynamics, Springer Series in Solid-State Sciences; Springer-Verlag: Berlin/Heidelberg, 2006; vol. 152.
42. Stoner, E.; Wohlfarth, E. Philos Trans R Soc Lond 1948, 240, 599.
43. Aharoni, A. J Appl Phys 1990, 68, 2892.
44. Feldtkeller, E.; Thomas, H. Z Phys B: Condense Matter 1965, 4, 8.
45. Guslienko, K. Y.; Novosad, V. J Appl Phys 2004, 96, 4451.
46. Usov, N. A.; Peschany, S. E. J Magn Magn Mater 1993, 118, L290.
47. Metlov, K. L.; Guslienko, K. Y. J Magn Magn Mater 2002, 242–245(Part 2), 1015.
48. Scholz, W.; Guslienko, K. Y.; Novosad, V.; Suess, D.; Schrefl, T.; Chantrell, R. W.; Fidler, J. J Magn Magn Mater 2003, 266, 155.
49. Landeros, P.; Escrig, J.; Altbir, D.; Laroze, D.; d'Albuquerque e Castro, J.; Vargas, P. Phys Rev B 2005, 71, 094435.
50. Usov, N. A.; Peschany, S. E. Fiz Met Metal 1994, 78, 13 (in russian).
51. Kravchuk, V. P.; Sheka, D. D.; Gaididei, Y. B. J Magn Magn Mater 2007, 310, 116.
52. Ha, J. K.; Hertel, R.; Kirschner, J. Phys Rev B 2003, 67, 224432.
53. Höllinger, R.; Killinger, A.; Krey, U. J Magn Magn Mater 2003, 261, 178.
54. The Object Oriented MicroMagnetic Framework. Availabel at: http://math.nist.gov/oommf/.
55. Caputo, J. G.; Gaididei, Y.; Kravchuk, V. P.; Mertens, F. G.; Sheka, D. D. Phys Rev B 2007, 76, 174428.
56. Thiele, A. A. Phys Rev Lett 1973, 30, 230.
57. Huber, D. L. Phys Rev B 1982, 26, 3758.
58. Mertens, F. G.; Bishop, A. R. In Nonlinear Science at the Dawn of the 21th Century; Christiansen, P. L.; Soerensen, M. P.; Scott, A. C., Eds.; Springer–Verlag: Berlin, 2000; p 137.
59. Guslienko, K. Y.; Novosad, V.; Otani, Y.; Shima, H.; Fukamichi, K. Appl Phys Lett 2001, 78, 3848.
60. Metlov, K. L. Two-dimensional topological solitons in small exchange-dominated cylindrical ferromagnetic particles, 2000, arXiv:cond-mat/0012146.
61. Guslienko, K. Y.; Metlov, K. L. Phys Rev B 2001, 63, 100403.
62. Guslienko, K. Y.; Ivanov, B. A.; Novosad, V.; Otani, Y.; Shima, H.; Fukamichi, K. J Appl Phys 2002, 91, 8037.
63. Metlov, K. L. Two-dimensional topological solitons in soft ferromagnetic cylinders, 2001, arXiv:cond-mat/0102311.
64. Ivanov, B. A.; Zaspel, C. E. J Appl Phys 2004, 95, 7444.
65. Zaspel, C. E.; Ivanov, B. A.; Park, J. P.; Crowell, P. A. Phys Rev B 2005, 72, 024427.
66. Guslienko, K. Y.; Han, X. F.; Keavney, D. J.; Divan, R.; Bader, S. D. Phys Rev Lett 2006, 96, 067205.
67. Ivanov, B. A.; Zaspel, C. E. Appl Phys Lett 2002, 81, 1261.

68. Ivanov, B. A.; Zaspel, C. E. Phys Rev Lett 2005, 94, 027205.
69. Kent, A. D.; Ozyilmaz, B.; del Barco, E. Appl Phys Lett 2004, 84, 3897.
70. Kent, A. D. Nat Mater 2007, 6, 399.
71. Xi, H.; Gao, K. Z.; Shi, Y. J Appl Phys 2005, 97, 044306.
72. Li, Z.; Zhang, S. Phys Rev Lett 2004, 92, 207203.
73. Shibata, J.; Nakatani, Y.; Tatara, G.; Kohno, H.; Otani, Y. Phys Rev B 2006, 73, 020403.
74. Liu, Y.; Gliga, S.; Hertel, R.; Schneider, C. M. Appl Phys Lett 2007, 91, 112501.
75. Liu, Y.; He, H.; Zhang, Z. Appl Phys Lett 2007, 91, 242501.
76. Sheka, D. D.; Gaididei, Y.; Mertens, F. G. In Electromagnetic, Magnetostatic, and Exchange-Interaction Vortices in Confined Magnetic Structures; Kamenetskii, E., Eds.; Research Signpost: India, 2008; p 59.
77. Waeyenberge, V. B.; Puzic, A.; Stoll, H.; Chou, K. W.; Tyliszczak, T.; Hertel, R.; Fähnle, M.; Bruckl, H.; Rott, K.; Reiss, G.; Neudecker, I.; Weiss, D.; Back, C. H.; Schütz, G. Nature 2006, 444, 461.
78. Xiao, Q. F.; Rudge, J.; Choi, B. C.; Hong, Y. K.; Donohoe, G. Appl Phys Lett 2006, 89, 262507.
79. Hertel, R.; Gliga, S.; Fähnle, M.; Schneider, C. M. Phys Rev Lett 2007, 98, 117201.
80. Lee, K. S.; Guslienko, K. Y.; Lee, J. Y.; Kim, S. K. Phys Rev B 2007, 76, 174410.
81. Kravchuk, V. P.; Sheka, D. D.; Gaididei, Y.; Mertens, F. G. J Appl Phys 2007, 102, 043908.
82. Komineas, S.; Papanicolaou, N. In Electromagnetic, Magnetostatic, and Exchange-Interaction Vortices in Confined Magnetic Structures; Kamenetskii, E., Eds.; Research Signpost: India, 2008.
83. Papanicolaou, N.; Spathis, P. N. Nonlinearity 1999, 12, 285.
84. Komineas, S.; Papanicolaou, N. Dynamics of vortex-antivortex pairs in ferromagnets. In Electromagnetic, Magnetostatic, and Exchange-Interaction Vortices in Confined Magnetic Structures; Kamenetskii, E., Eds.; Research Signpost: India, 2008; p 335.
85. Komineas, S. Phys Rev Lett 2007, 99, 117202.
86. Belavin, A. A.; Polyakov, A. M. JETP Lett 1975, 22, 245
87. Hertel, R.; Schneider, C. M. Phys Rev Lett 2006, 97, 177202.
88. Tretiakov, O. A.; Tchernyshyov, O. Phys Rev B 2007, 75, 012408.
89. Gradshteyn, I. S.; Ryzhik, I. M. Table of Integrals, Series and Products; Elsevir, Inc., 1980.